PAPER • OPEN ACCESS

Estimation of roughness effects on wind turbine blades with vortex generators

To cite this article: A K Ravishankara et al 2020 J. Phys.: Conf. Ser. 1618 052031

View the <u>article online</u> for updates and enhancements.



IOP ebooks™

Bringing together innovative digital publishing with leading authors from the global scientific community.

Start exploring the collection-download the first chapter of every title for free.

1618 (2020) 052031

doi:10.1088/1742-6596/1618/5/052031

Estimation of roughness effects on wind turbine blades with vortex generators

A K Ravishankara^{1,2}, I Bakhmet¹ and H Özdemir¹

E-mail: akshay.koodlyravishankara@tno.nl, iana.bakhmet@tno.nl, huseyin.ozdemir@tno.nl

Abstract. Surface degradation of the wind turbine blades lead to a reduction while on the other hand blade add-ons like, vortex generators, lead to an increase in the aerodynamic performance. Within this study, both the reduction due to leading edge roughness and the increase due to vortex generators in the aerodynamic performance are quantified individually first, and then it is investigated if the vortex generators would compensate for the losses due to roughness. Roughness models for the Spalart-Allamaras (SA) and $k-\omega$ SST turbulence models are implemented in the open source CFD suite SU2 and validated against theoretical predictions and experimental data. The roughness model is then applied to a commonly used airfoil section, DU97-W-300 and steady RANS simulations are carried out with SU2. Four different conditions are considered - no erosion (clean), eroded (rough), clean blade section with VGs and rough blade section with VGs. Numerical simulations are validated with experimental data for the clean airfoil section and airfoil section equipped with vortex generators. Finally, a preliminary analysis is presented for each of the cases considered on the effect of power production.

1. Introduction

The subject of leading edge erosion is gaining significance in wind turbine industry in the recent years. The combination of growth in the size of wind turbines, increased offshore installations especially in locations with more adverse weather conditions has made this subject crucial to the industry[1]. Erosion of turbine blades is largely caused by rain, hailstones, accumulation of contaminants which tends to change the shape of the airfoils. This leads to a reduction in aerodynamic performance of the affected sections. Han[2] recently presented the effects of contamination of the airfoil used at blade tips on a 5MW NREL turbine blade using CFD simulations. They report a worst case scenario where the Annual Energy Production (AEP) drops by 3.7%. Herring[1] present a thorough review on the growing importance of leading edge erosion and different coating alternatives to reduce the impact of erosion. A wide range of drop in AEP, from about 25% to about 3.7%, is reported and the authors suggest it is due to different operating conditions and roughness levels used to evaluate the impact of erosion. The authors also note that repair of moderate erosion can uplift the AEP by about 2%.

¹ TNO, Petten, The Netherlands

² University of Twente, Enschede, The Netherlands

Content from this work may be used under the terms of the Creative Commons Attribution 3.0 licence. Any further distribution of this work must maintain attribution to the author(s) and the title of the work, journal citation and DOI.

1618 (2020) 052031

doi:10.1088/1742-6596/1618/5/052031

Vortex Generators (VG) are commonly used to delay stall of an airfoil since they prevent early separation of the flow. Typically placed on the suction side of the airfoils (usually between $x/c \approx 0.2$ to 0.3), VGs help delay separation of the flow by mixing high energy external flow with the boundary layer. VGs are generally most effective at higher angles of attack (e.g. see task 4.8 in AVATAR[3]) and by keeping the flow attached to the airfoil, they can delay stall and also increase the maximum lift produced. However, the drag also increases at lower angles of attack.

In this paper, we explore different methods to model the effect of surface roughness in RANS simulations and investigate the performance of a VG in rough conditions. Due to leading edge erosion, the nature of the turbulent boundary layer changes. There is additional dissipation near the roughness elements which leads to thickening of the boundary layer. The loss in momentum makes the boundary layer prone to early separation. However, the VG adds momentum to the boundary layer by mixing external flow thus, in principle, overcoming the negative effects of leading edge erosion. For the final application, the DU97W300 airfoil which is used in the AVATAR[3] turbine blade is chosen.

The organization of the paper is as follows: section 2 gives some information about SU2, the CFD solver for the numerical simulations. In Section 3 two different roughness models for RANS are presented with validation cases. Finally, in section 4, the effect of VG on rough airfoil (DU97W300) is presented.

2. Numerical method

2.1. SU2

SU2, the CFD solver used in this study, is an open-source collection of C++ based software tools for performing Partial Differential Equation (PDE) analysis and solving PDE-constrained optimization problems[4]. Originally developed for aerospace applications, the solver has been extended for incompressible flows. In this study, we use the low Mach preconditioned incompressible flow solver[5]. The governing equations of SU2 are written in the general form:

$$\partial_t U + \nabla \cdot \vec{F}^c - \nabla \cdot \vec{F}^v = Q \quad \text{in} \quad \Omega, \quad t > 0,$$
 (1)

where U is the vector of conservative variables, \vec{F}^c are the convective flux, \vec{F}^v are the viscous flux and Q is a source term defined as

$$U = \begin{bmatrix} \rho \\ \rho u_1 \\ \rho u_2 \\ \rho u_3 \\ \rho c_P T \end{bmatrix}, \quad \vec{F}_i^c = \begin{bmatrix} \rho u_i \\ \rho u_i u_1 + P \delta_{i1} \\ \rho u_i u_2 + P \delta_{i2} \\ \rho u_i u_3 + P \delta_{i3} \\ \rho u_i c_P T \end{bmatrix}, \quad \vec{F}_i^v = \begin{bmatrix} 0 \\ \tau_{i1} \\ \tau_{i2} \\ \tau_{i3} \\ \kappa \nabla T \end{bmatrix}.$$
 (2)

In equation 2, $\vec{v} = (u_1, u_2, u_3)$ is the velocity vector, ρ is the density, P is the dynamic pressure and the viscous stresses are $\tau_{ij} = \mu_{tot} (\partial_j v_i + \partial_i v_j - \frac{2}{3} \delta_{ij} \nabla \cdot \vec{v})$. The total viscosity coefficient, μ_{tot} is the sum of the dynamic viscosity μ_{dyn} and turbulent viscosity μ_{tur} , which is computed via a turbulence model. c_P is the specific heat at constant pressure, T is the temperature and κ is the thermal conductivity. The Spalart-Allmaras (SA) and the Mean Shear Stress Transport (SST) turbulence models can be used to compute μ_{tur} . More details can be found in [5].

2.1.1. Spatial discretization The spatial discretization is performed on an edge based dual grid using a finite volume approach. An upwind Flux Difference Splitting (FDS) scheme is used to find the convective flux residual. The MUSCL scheme is used to obtain second order accuracy. Flux reconstruction is performed by gradients computed using the Weighted Least

1618 (2020) 052031

doi:10.1088/1742-6596/1618/5/052031

Squares method. The gradients required for fluxes to evaluate viscous flux is computed using either the Least Squares method or the Green Gauss theorem.

2.1.2. Time discretization Steady state problems are also solved using a pseudo-time stepping approach where the solution is marched in time until convergence. Time integration is carried out using the Implicit Euler method.

2.2. Turbulence modeling

2.2.1. Spalart-Allamaras (SA) The SA model can be written in the general form of equation 1 as

$$U = \tilde{\nu}, \qquad \vec{F}^c = u_i \tilde{\nu}, \qquad \vec{F}^v = \frac{(\nu + \tilde{\nu})}{\sigma} \partial_j \tilde{\nu}, \qquad Q = c_{b1} \tilde{S} \tilde{\nu} - c_{w1} f_w \left(\frac{\tilde{\nu}}{d_S}\right)^2 + \frac{c_{b2}}{\sigma} |\partial_j \tilde{\nu}|^2.$$
 (3)

The turbulent viscosity is then computed as

$$\mu_{tur} = \rho \tilde{\nu} f_{v1}, \quad f_{v1} = \frac{\chi^3}{\chi^3 + c_{v1}^3}, \quad \chi = \frac{\tilde{\nu}}{\nu}, \quad \tilde{S} = \Omega + \frac{\tilde{\nu}}{\kappa^2 d^2} f_{v2}, \quad f_{v2} = 1 - \frac{\chi}{1 + \chi f_{v1}}.$$
 (4)

Here $\nu = \frac{\mu}{\rho}$ is the dynamic viscosity, d is the distance to the nearest wall. The definitions of the other model constants can be found in the literature [6, 7].

2.2.2. SST~k- ω Following the general form of the equations in equation 1, the corresponding terms for the SST k- ω model are

$$U = \begin{bmatrix} \rho k \\ \rho \omega \end{bmatrix}, \vec{F}^c = \begin{bmatrix} \rho u_i k \\ \rho u_i \omega \end{bmatrix}, \vec{F}^v = \begin{bmatrix} (\mu + \sigma_k \mu_t) \partial_i k \\ (\mu + \sigma_\omega \mu_t) \partial_i \omega \end{bmatrix} Q = \begin{bmatrix} P - \beta^* \rho \omega k \\ \frac{\gamma}{\nu_t} P - \beta \rho \omega^2 + 2(1 - F_1) \frac{\rho \sigma}{\omega} \partial k_i \partial \omega_i \end{bmatrix}.$$
(5)

Here $P = \tau_{ij} \frac{\partial u}{\partial x_j}$, where τ_{ij} is defined earlier in section 2.1, ρ is density, $\nu_t = \mu_t/\rho$ is the dynamic turbulent viscosity and μ is laminar viscosity. The turbulent eddy viscosity is computed as

$$\mu_t = \frac{\rho a_1 k}{\max(a_1 \omega, \Omega F_2)}.$$
 (6)

Model constant definitions can be found in various literature[4, 8]

3. Roughness modeling

In this study, we aim to model the impact of roughness by qualitatively mimicking the behavior of the flow around these roughness elements. In order to motivate the roughness model used in the present study, a brief introduction of turbulent boundary layers and how roughness impacts the boundary layer is presented below.

The turbulent boundary layer can be broadly divided into two regions [9, 10]; the inner region where viscous dissipation is comparable to the turbulent dissipation and the outer region where turbulence dissipation dominates completely. The inner region can be further subdivided into three regions - the viscous sublayer where viscous effects dominate and turbulent effects are absent, a buffer region where the turbulent stresses start to grow and finally an overlap region or a logarithmic overlap region where the turbulent and viscous dissipation match. The overlap region leads into the outer layer of the boundary layer where viscous effects are minimal. The velocity profile in the viscous sublayer and overlap region can be written respectively as

$$u^+ = y^+, y^+ \le 5,$$
 (7)

1618 (2020) 052031

doi:10.1088/1742-6596/1618/5/052031

$$u^{+} = \frac{1}{\kappa} log(y^{+}) + C, \qquad y^{+} > 30.$$
 (8)

The region of the boundary layer between $5 \le y^+ \le 30$ is the buffer region. In the above relations, y^+ is the stretched wall normal coordinate and u^+ is the normalized velocity defined as

$$y^+ = \frac{yu_\tau}{\nu}, \qquad u^+ = \frac{u}{u_\tau}, \qquad u_\tau = \sqrt{\frac{\tau_w}{\rho}},$$

Here u_{τ} is known as the wall friction velocity and is used as the velocity scale close to the wall, τ_w is the wall shear stress, ρ is the density, u is the local velocity and ν is the dynamic viscosity. The constant in equation 8 for a smooth wall is known to be C = 5.0.

The presence of surface roughness on the wall alters the nature of the velocity distribution near the wall. The roughness elements will introduce new turbulent fluctuations in the flow increasing the skin friction among other things. Typically, a standardized notion of roughness known as the "equivalent sand grain roughness height (k_s)" is used to denote roughness of a wall [9, 11, 12]. A given physical roughness distribution is converted into the "equivalent sand grain roughness height" using empirical correlations[13, 14, 15]. Based on the stretched roughness height $k_s^+ = k_s u_\tau / \nu$ three regimes of roughness can be identified[9]:

- (i) Hydraulically smooth for $k_S^+ \leq 5$,
- (ii) Transitionally rough for $5 \le k_S^+ \le 70$,
- (iii) Fully rough for $k_S^+ > 70$.

If the roughness elements are within the viscous sublayer $(k_S^+ \leq 5)$, effect of roughness is not relevant and there is no difference between the smooth velocity profile. As the height of the roughness element increases $(5 \leq k_S^+ \leq 70)$, a shift in the velocity profile is observed. Once the roughness elements are fully within the overlap region $(k_S^+ > 70)$, the viscous sublayer plays no part and the flow is in the fully rough regime. It must be noted here that the equivalent sand grain roughness concept typically applies only to a distributed roughness (k- type roughness[16]). To reproduce the proper shift Δu^+ in the boundary layer velocity profiles, turbulence models typically increase the eddy viscosity dissipation within the inner part of the boundary layer [12]. Aupoix et al.[12], identify two methods to accomplish this with eddy viscosity based turbulence models (like SA and SST):

- (i) Finite eddy viscosity at the wall which can be interpreted as using a virtual wall to represent roughness and
- (ii) Zero eddy viscosity at the wall where the origin of the wall is at the bottom of roughness but turbulence damping in the wall region is reduced.

With this background on roughness modeling in turbulent boundary layers, roughness models for the SA and SST turbulence models are presented.

3.1. Roughness modification for SA model

The roughness modification proposed by Boeing [7, 12] is considered in this section. An alternate modification was also proposed by ONERA in Aupoix et al.[12] but is not considered since it requires the additional input of friction velocity. The effect of roughness is accounted for by shifting the virtual wall to the top of the roughness element. This can be achieved by offsetting the distance to the wall everywhere. The changes to the turbulence model are

$$d_{new} = d_{min} + 0.03k_S.$$
 $\chi = \frac{\tilde{\nu}}{\nu} + c_{R1} \frac{k_S}{d_{new}},$ $f_{v2} = 1 - \frac{\tilde{\nu}}{\nu + \tilde{\nu} f_{v1}}.$ (9)

1618 (2020) 052031

doi:10.1088/1742-6596/1618/5/052031

with $c_{R1} = 0.5$. The eddy viscosity at the wall is now changed from $\tilde{\nu} = 0$ to a non-zero value by using a mixed boundary condition at the wall,

$$\left. \frac{\partial \tilde{\nu}}{\partial n} \right|_{wall} = \frac{\tilde{\nu}_{wall}}{0.03k_S},$$
(10)

where $\frac{\partial \tilde{\nu}}{\partial n}$ is the gradient of $\tilde{\nu}$ in the direction normal to the wall.

3.2. Roughness modification for SST model

The effect of roughness can be accounted for in the $k - \omega$ SST turbulence model by modifying the boundary conditions at the wall as[8]

$$k = 0, (11)$$

$$\omega_{rough} = \frac{(\mu_{\tau})^2 S_R}{\nu},\tag{12}$$

where

$$S_R = \begin{cases} (\frac{50}{k^+})^2, & k^+ \le 25, \\ (\frac{100}{k^+}), & k^+ > 25. \end{cases}$$

From equation 6, the eddy viscosity remains zero at the wall, but there is an increase in turbulence dissipation compared to the clean boundary conditions.

The two roughness models are implemented in SU2 and are validated below.

3.3. Turbulent flow over a 2-D flat plate

Turbulent flow over a flat plate with different roughness heights is simulated with both the SA and the SST turbulence models and their respective roughness corrections presented above. The velocity profiles for different roughness heights are presented in figure 1. The flat plate domain is 2m long and $Re = 6.0 \times 10^6$. A minimum $y^+ = 0.4$ is maintained on the flat plate. There are 113 points on the surface of the 2-D flat plate and the minimum grid spacing is 2×10^{-6} .

From figure 1, we can see that the clean case matches the viscous sublayer and log law in the overlap region closely for both the SA and SST models. Further, increasing the equivalent roughness height has the predicted effect of shift of the velocity profile away from the clean case and once $k^+ > 70$, the viscous sublayer disappears.

To further verify the two results, a comparison is made with the theoritical shift in velocity profile as proposed by Nikuradse[17]. On comparison to theoretical predictions of the velocity shift (figure 1), a slight over-prediction is observed in the transitionally rough region by the SA roughness model. This was also reported in Knopp et al[18]. The SST roughness model does not perform as well as the SA model especially in the fully rough regime. Additionally, due to other limitations in the $k-\omega$ SST roughness model reported elsewhere[17, 18, 19]. The roughness heights due to leading edge erosion is likely to span all the regimes of roughness at various stages of erosion and in order to ensure that even fully rough cases can be adequately modeled, the SA model is chosen for further analysis. It must be noted that various corrections for the SST roughness model have been proposed but are not investigated in the current study.

3.4. Blanchard experiments

In this section, two roughness models are compared to the experimental data from Blanchard. The experimental data from Blanchard is obtained from Aupoix et al[12]. The sand grain roughness height was 0.000425m. With an incoming velocity of $45ms^{-1}$, the simulation is carried out on a 2m long flat plate. The resulting $Re = 6.46 \times 10^6$. The y^+ of the mesh used

1618 (2020) 052031

doi:10.1088/1742-6596/1618/5/052031

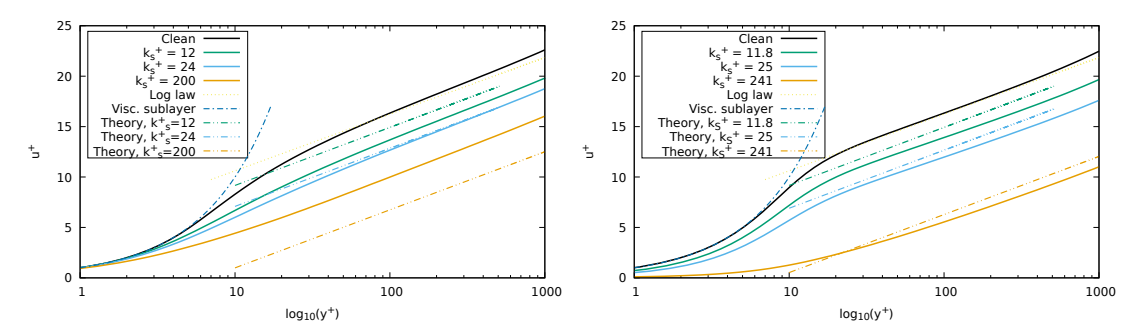


Figure 1. A comparison of velocity shifts obtained from SST(left) and SA(right) models to the theoretical value.

is less than 0.4 throughout the domain. The comparison is shown in figure 2. Both the SA and SST models predict a higher skin friction than a clean flat plate but the results from SA roughness model is closer to the experimental data. The resulting $k_s^+ \approx 150$ makes the flow fully rough. As seen in figure 1, the SST roughness model performs poorly in this regime which results as an under prediction of the skin friction further justifying the choice of SA model in this study.

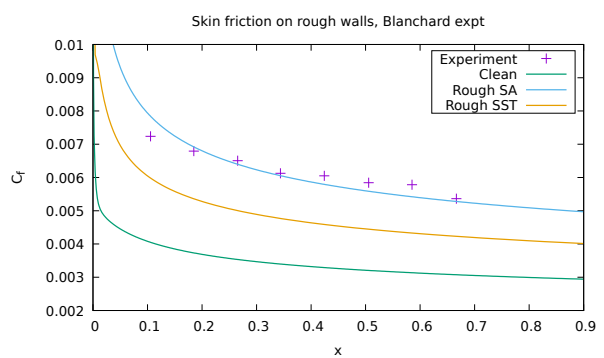


Figure 2. Comparison of skin friction coefficient (C_f) from SST and SA roughness models to experimental data from Blanchard.

3.5. NACA 65₂215 airfoil validation

The SA model is further validated against the NACA 65_2215 airfoil. The Re is 2.6×10^6 and the roughness covers the entire upper surface and on the lower surface from the leading edge up to x/c = 0.15. Three roughness heights - $k_S/c = 1.54 \times 10^{-4}$, $k_S/c = 3.08 \times 10^{-4}$ and $k_S/c = 1.23 \times 10^{-3}$ are considered here. Experimental data is obtained from Abbot and Doenhoff[20]. Ljungstrom performed experiments with different roughness heights on the NACA 65_2A215 airfoil, a closely related airfoil. These experiments have been used to validate roughness models by Knopp[18] and Hellsten[21] previously. The data from Ljungstrom are also taken from the same references.

A two dimensional C-grid topology is used for all the simulations. Grid refinement study is carried out at an angle of attack of 8° on meshes with 150, 250 and 450 nodes on the airfoil surface. A $y^{+} < 1$ is maintained for the three grids. The resulting lift and drag coefficients are listed in table 1. Based on the results in table 1, the grid with 250 points on the airfoil was used for further computations. The farfield and wall boundary conditions are applied at the edge of the domain and on the airfoil respectively.

The left figure 3 shows the comparison of numerical results from the SA model under clean conditions and a roughness height of $k_s/c = 1.23 \times 10^{-3}$. The numerical results from SU2

1618 (2020) 052031

doi:10.1088/1742-6596/1618/5/052031

N	C_l	C_d	
150	1.0273	0.0149	
250	1.0336	0.0141	
450	1.0346	0.0138	

Table 1. Lift and Drag coefficients with different grid resolutions for the NACA 65₂215 airfoil.

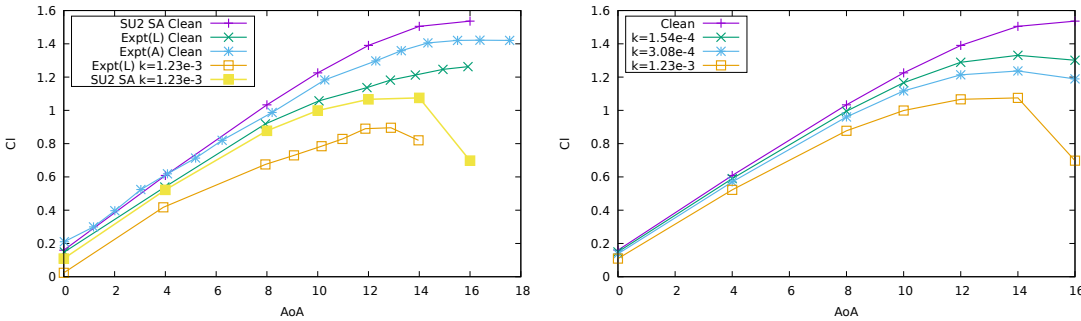


Figure 3. Comparison of NACA 65_2215 polars against experiments (left) and numerical results with different roughness heights (right). Expt(L) referes to results from Ljungstrom and Expt(A) from Abbot and Doenhoff[20].

compare very well against the data from Abbot[20] at lower angles of attack but SU2 over predicts the maximum lift. This could be due to a later prediction of flow separation by SA turbulence model compared to the experiments. Since no experimental pressure data is available, this cannot be confirmed. However, the lift values reported by Ljungstrom are significantly lower. Since the two airfoils under consideration are supposed to be very similar, Hellsten[21] concludes that lift values reported by Ljungstrom are too low likely due to imperfections from a retracted flap in airfoil geometry setup. The absolute values of the lift coefficients do not compare well against Ljungstrom, but considering the comments of Hellsten the trends observed due to roughness is similar. The maximum lift is observed around an angle of attack of 16° for the clean case in both numerical and experimental data. The addition of roughness causes a reduction in maximum lift by 28.8% in SU2 and by 29.3% in the experimental results reported. However, SU2 predicts a higher value for the angle at which the maximum lift occurs compared to experiments. This is again likely due to later prediction of separation point by the SA model.

On the right of figure 3 the predicted lift coefficients with different roughness heights are shown. With increasing roughness, the maximum lift value and the angle at which this occurs decreases. Based on the computed skin friction values at an angle of attack of 8° , k_s^+ varies from 70 to about 850. These values suggest the flow is likely to be fully rough but it will vary depending on the flow conditions. Due to some of the defecincies observed with the SST roughness model at larger k_s^+ values previously, only the SA model is used in this work.

4. Roughness on turbine blade sections

A typical wind turbine airfoil, DU-97-300, is chosen to test the effect of roughness and verify if VGs can alleviate the anticipated drop in performance. This choice is motivated by the availability of experimental data for clean and VG cases. The geometry of the VG is chosen from the AVATAR experimental database (figure 4)[22, 23]. The simulations are carried out at $Re = 2.0 \times 10^6$ for both clean and VG cases. Both for clean and VG cases a 3D mesh is generated where the airfoil is extruded in span direction and a body-fitted mesh is generated around the VG geometry. A symmetry boundary condition is used on the spanwise extrusion

1618 (2020) 052031

doi:10.1088/1742-6596/1618/5/052031

boundaries.

The following cases are considered:

- (i) Airfoil with no roughness or VGs under fully turbulent conditions (denoted as 'clean'),
- (ii) Airfoil with VG under fully turbulent conditions ('VG'),
- (iii) Airfoil with roughness ('rough') and
- (iv) Airfoil with VG and roughness ('VGrough').

For the clean airfoil, a grid refinement study is carried out at $AoA = 2.5^{\circ}$, which corresponds to the design angle of attack of this airfoil section on the AVATAR reference turbine blade under normal operating conditions (incoming wind speed of 10m/s). The coarsest grid has 128 points (lvl1), the reference grid (lvl2) has 300 points and the finest grid (lvl3) has 512 points on the airfoil and 4 points in the span direction. Figure 4 shows the vortex generator on the airfoil section and details of the geometry. For the airfoil with VG (zero thickness), 1000 points are used on the airfoil and 15 points in the span direction (a maximum aspect ratio of 3 and an average of 1.15 is maintained on the airfoil surface) and no refinement study is made. The VG geometry is also shown in figure 4. The corresponding dimensions are h = 5mm, D = 35mm, d = 17.5mm and $\beta = 15^{\circ}$. The chord length of the airfoil is 0.65m and the VG is placed at 20% chord on the upper surface of the airfoil[23]. Since a symmetry boundary condition is used on the extrusion boundaries, the geometry represents a row of counter-rotating VGs as shown in the right figure 4.

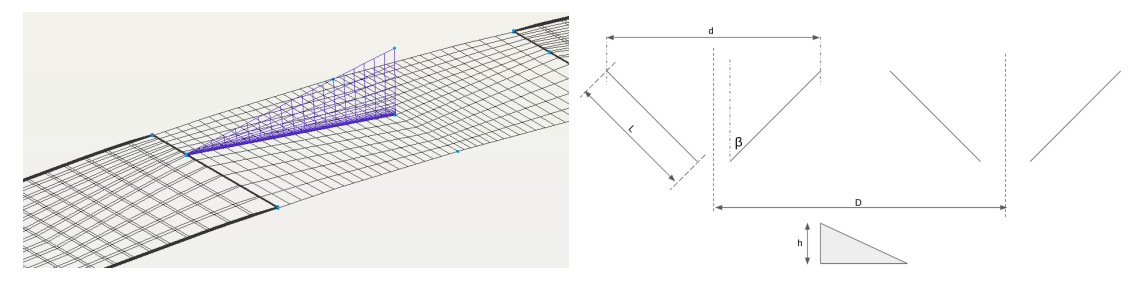


Figure 4. VG on the airfoil surface (left) and VG geometry details [23](right)

Figure 5 shows the pressure coefficient and skin friction coefficient along the airfoil obtained from the three grids. The results from reference grid and fine grid are mostly identical and thus the reference grid will be used for further computations. The resulting lift and drag coefficients are listed in table 2. Only fully turbulent cases are considered for comparison here because the roughness model does not predict the early onset of transition.

Name	N	C_l	C_d
lvl1	128	0.5308	0.0180
lvl2	300	0.5011	0.0161
lvl3	512	0.5077	0.0160

Table 2. Lift and Drag coefficients with different grid resolutions for the DU-97-W300 airfoil.

4.1. Clean polars

Figure 6 shows the lift and drag polars from SU2 and the experimental data from Baldaccino[23]. Additionally, the lift data from other CFD methods obtained from Avatar report[22] is also

1618 (2020) 052031

doi:10.1088/1742-6596/1618/5/052031

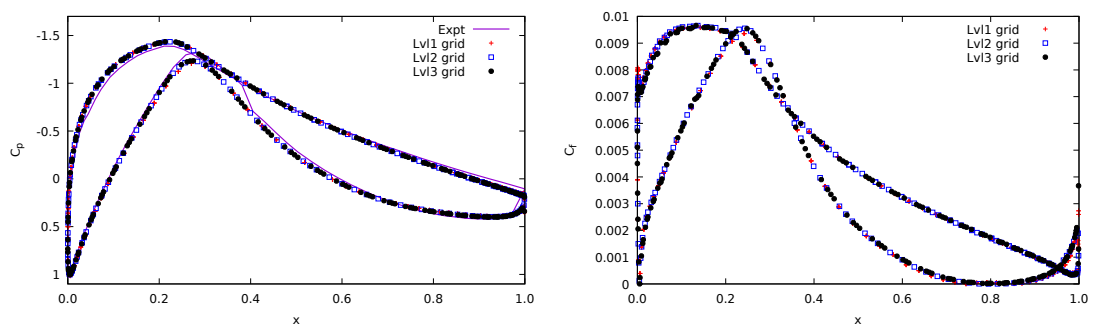


Figure 5. Comparison of the pressure coefficient (left) and the skin friction coefficient (right) at an $AoA = 2.5^{\circ}$, $Re = 2.0 \times 10^{6}$ for different grid resolutions.

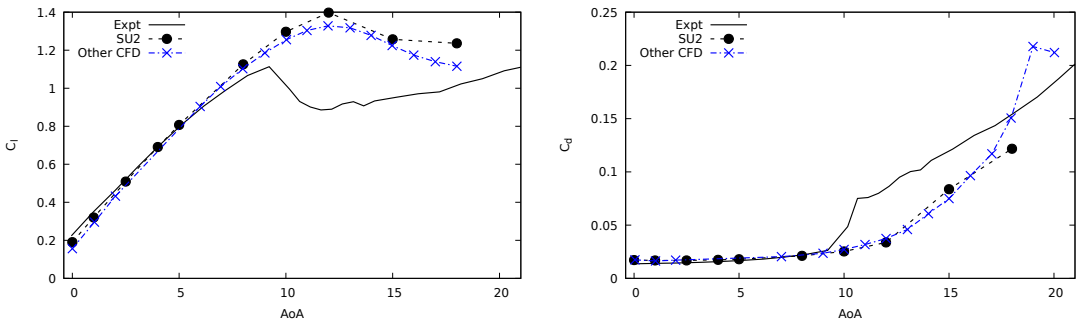


Figure 6. Lift (left) and drag (right) polars for the fully turbulent (clean) case at $Re = 2.0 \times 10^6$.

given. The maximum lift angle and the maximum C_l is over estimated by CFD compared to experiments. However, the results from SU2 are in close agreement to those reported by Ellipsys in AVATAR[3] (task 3.2). Similar behavior is observed for C_d as well. The SA model predicts the separation to occur later than the experiments which results in poor performance at higher angles of attack and over prediction of maximum lift. While the use of psuedo time stepping scheme helps overcome some of the convergence issues that a purely steady-state solver would face at higher angles of attack, accuracy of the results remains poor.

4.2. VG polars

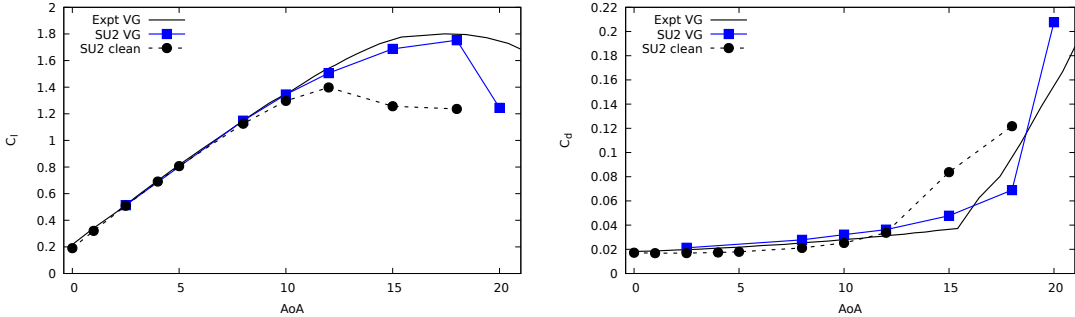


Figure 7. Lift (left) and drag (right) polars for the fully turbulent case at $Re = 2.0 \times 10^6$ with VG (VG).

Figure 7 shows the comparison of lift and drag polars from SU2 with experimental data[23] at $Re = 2 \times 10^6$ under fully turbulent conditions. Good agreement between the numerical and experimental data is observed at lower angles of attack. SU2 underpredicts the value of the

1618 (2020) 052031

doi:10.1088/1742-6596/1618/5/052031

maximum C_l but the stall angle is over predicted. In section 4.1, the stall angle predicted by SU2 is around 12° which is higher than the experimentally obtained value. From figure 7 we observe that the addition of the VG has delayed the stall until an $AoA = 18^{\circ}$ as expected. A very close match is observed at lower angles but deviations increase at higher angles of attack. Looking at the drag polar on right the SA model once again predicts separation to occur later than the experiments. However, the maximum lift and the stall angle prediction is much better with VGs than compared to the fully turbulent clean case.

4.3. Roughness effects

Determination of the appropriate value of roughness height, k is difficult due to lack of experimental data for the airfoil under consideration in rough conditions. Additionally, since no transition model is used in this study, the roughness height used must ideally trigger a very early onset of transition to ensure the flow remains turbulent over the airfoil. Several studies on isolated 3-D roughness elements have reported a critical $Re_{k,crit} > 600[16]$ based on the roughness height, k, which induce larger instabilities in the flow that trigger transition at the location of roughness or even upstream. The study on critical values for distributed roughness is an ongoing research problem [16]. In this paper, we use a value of the roughness height to ensure that $Re_k = 800$. Once the roughness height, k, is defined, an equivalent sand grain roughness height, k_s , must be estimated. Langel et al. [24] assume $k_s/k = 1$ for densely packed roughness distribution and a lower value of $k_s/k \approx 0.47$ for lower density (15% distribution density). Aupoix et al.[12] use correlations from Dirling[13] to estimate k_s/k . Following the Dirling's correlation and assuming the distributed roughness to be closely spaced we find $k_s/k \approx 0.539$ which is used to specify the input for turbulence model considered in this study. Based on these estimates, $k_s/c = 400.0 \times 10^{-6}$ is used. In order to mimic leading edge erosion, the airfoil surface from the leading edge to x/c = 0.13 on the pressure side and from leading edge to x/c = 0.02on the suction side is assumed to be rough.

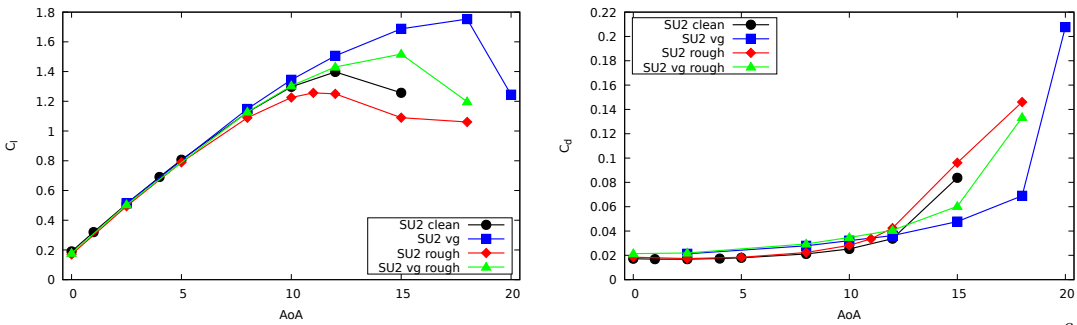


Figure 8. Lift (left) and drag (right) polars for the fully turbulent case at $Re = 2.0 \times 10^6$ under different conditions ('clean' -black, 'VG' - blue, 'rough' - red, 'VGrough' - green).

The addition of roughness causes a reduction in the lift and increase in drag compared to the clean case (the black and red curves in figure 8). Based on the computed wall shear stress values the resulting $k_s^+ \approx 240$ corresponds to the fully rough regime. Despite a fairly moderate choice of roughness height (keeping transition in mind), the flow is already in the fully rough regime. Additionally, the airfoil appears to stall slightly earlier due to presence of roughness. Adding a VG on the rough airfoil appears to counteract some of the negative effect of roughness by increasing the lift, however the drag increases further. The VG does delay the stall and the airfoil now stalls at approximately 15° even with leading edge roughness.

A clearer picture emerges when we investigate the pressure coefficient in different cases (figure 9). At an $AoA = 12^{\circ}$, the fully turbulent (clean) flow is separated close to the trailing edge

1618 (2020) 052031

doi:10.1088/1742-6596/1618/5/052031

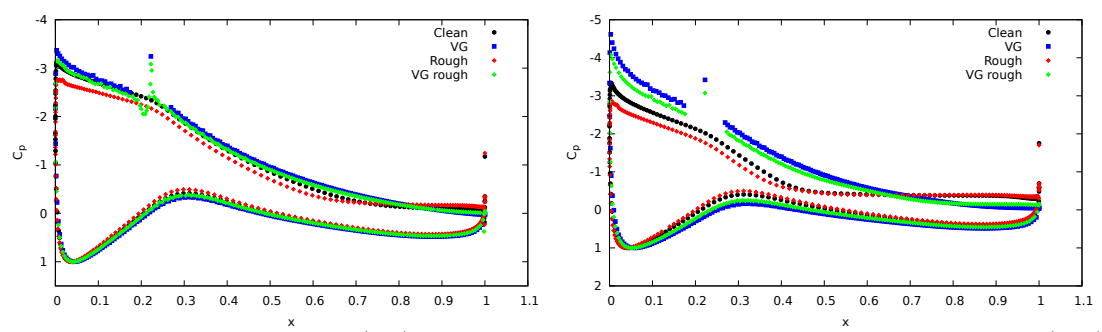


Figure 9. Pressure coefficient (C_p) distribution under different cases at $AoA = 12^{\circ}$ (left) and $AoA = 15^{\circ}$ (right).

around x/c = 0.9. This angle of attack also corresponds to the maximum C_l . Under rough conditions, the flow separates much earlier however, the VG helps the flow to remain attached throughout. The difference is clearer when examining the C_p for $AoA = 15^{\circ}$ in figure 9. Under both 'clean' and 'rough' conditions, the airfoil is under stall. Flow remains attached longer with the VG as expected under both clean and rough conditions.

4.4. Aerodynamic efficiency

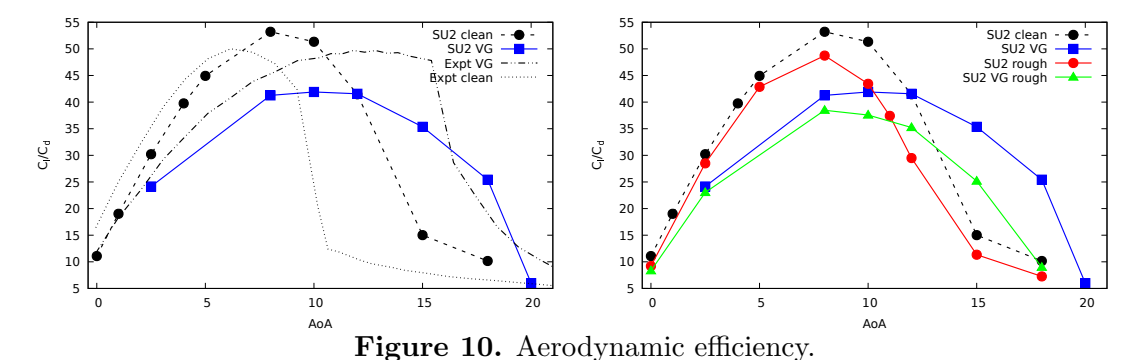


Figure 10 shows the aerodynamic efficiencies under different conditions. On the left, the comparison between numerical SU2 results and experiments are shown. There is an under prediction of efficiency at lower angles of attack due to over prediction of drag. As also seen in the lift polar results, there is an over prediction in maximum efficiency and the angle where it occurs. However, in the VG case, there is a consistent under prediction in efficiency due to over prediction of drag coefficients. Comparing the clean and VG cases, the efficiency at lower angles is lower with VG due to additional drag but at higher angles of attack (beyond stall), the efficiency with VGs remains high as expected. On the right, the comparison of efficiencies with roughness is shown. Due to roughness, a reduction in efficiency is observed both with and without VGs as expected. The maximum efficiency is also reduced in both cases. At higher angles of attack, the VG increases the efficiency even under rough conditions.

4.5. Power analysis

A preliminary analysis of the effect of roughness on the AVATAR wind turbine blade [3] at an incoming wind velocity of 10m/s is performed using Blade Element Momentum theory with the Blade Optimization Tool (BOT) developed in-house. With the 'rough' case, a drop of 2.5% is observed compared to the 'clean' section. The addition of VG however did not appreciably change the power output when compared to a rough surface. This is likely because the operating

1618 (2020) 052031

doi:10.1088/1742-6596/1618/5/052031

angle of attack for this airfoil is in the linear region where the VG does not have a beneficial effect on aerodynamic performance. We should note that, the CFD analysis are performed for the Re number of 2.0×10^6 where we could clearly see the effects of VGs on the rough surface but, the power analysis (BOT) are performed for the operating conditions of AVATAR blade where the Re number is around 10.0×10^6 . The polar data for BOT is synthesized from the provided CFD data.

5. Conclusions

In this paper, different roughness models for the SA and SST turbulence models are tested for flat plates. The effect of leading edge erosion is then investigated on the DU97-W-300 airfoil section using the roughness models. It is clear that surface degradation leads to reduction in aerodynamic performance as the flow tends to separate earlier which can even lead to premature stall. A reduction of $\approx 2.5\%$ in power production is observed under rough conditions compared to clean conditions. Addition of the vortex generator appears to counter act the negative effects of roughness and is most effective at higher angles of attack. However, due to the presence of the vortex generator drag increases further under rough conditions. The addition of the VG did not appreciably change the power produced by the rotor compared to a rough surface where the polar data that are used for the power analysis are synthesized.

References

- [1] Herring R, Dyer K, Martin F and Ward C 2019 Renewable and Sustainable Energy Reviews 115 109382
- [2] Han W, Kim J and Kim B 2018 Renewable Energy 115 817–823
- [3] AVATAR 2017 Avatar: Results and deliverables http://eera-avatar.eu/publications-results-and-links/index.html, Last accessed on 2020-02-24
- [4] Palacios F, Padron S, Tracey B, Manosalvas D E, Aranake A, Copeland S R, Variyar A, Alonso J J, Lukaczyk T W, Lonkar A K, Naik K R and Economon T D 2014 52nd Aerospace Sciences Meeting AIAA 2014-0243
- [5] Economon T D 2019 AIAA Journal **58:2** 1–13
- [6] Spalart P and Allmaras S 1992 30th aerospace sciences meeting and exhibit AIAA 1992-439
- [7] Spalart P 2000 Fluids 2000 Conference and Exhibit AIAA 2000-2306
- [8] Wilcox D C 2006 (Canada: DCW Industries)
- [9] Schlichting H and Gersten K 2016 (Berlin Heidelberg: Springer-Verlag)
- [10] Pope S B 2000 (Cambridge University Press)
- [11] Nikuradse J 1950 (National Advisory Committee for Aeronautics Washington)
- [12] Aupoix B and Spalart P 2003 International Journal of Heat and Fluid Flow 24 454-462
- [13] Dirling JR R B 1973 8th Thermophysics Conference p 763
- [14] Grabow R and White C 1975 AIAA Journal 13 605–609
- [15] Braslow A L and Knox E C 1958 Tech. Rep. NACA-TN-4363
- [16] Langel C M, Chow R, Dam C P v, Rumsey M A, Maniaci D C, Ehrmann R S and White E B 2014 52nd Aerospace Sciences Meeting AIAA 2014-0234
- [17] Aupoix B 2015 Journal of Fluids Engineering 137:2
- [18] Knopp T, Eisfeld B and Calvo J B 2009 International Journal of Heat and Fluid Flow 30 54-65
- [19] Aupoix B 2014 10th International ERCOFTAC Symposium on Engineering Turbulence Modelling and Measurements hal-01071701
- [20] Abbott I H and Von Doenhoff A E 2012 Theory of wing sections: including a summary of airfoil data (New York: Dover Publications)
- [21] Hellsten A, Laine S, Hellsten A and Laine S 1997 22nd Atmospheric Flight Mechanics Conference p 3577
- [22] Schepers J, Boorsma K, Sørensen N, Voutsinas, Sieros G, Rahimi H, Heisselmann H, Jost E, Lutz T, Maeder T, Gonzalez A, Ferreira C, Stoevesandt B, Barakos G, Lampropoulos N, Croce A and Madsen J 2018 Journal of Physics: Conference Series 1037 022013
- [23] Baldacchino D, Ferreira C, Tavernier D D, Timmer W and van Bussel G 2018 Wind Energy 21 745-765
- [24] Langel C M, Chow R, Hurley O F, Dam C P v, Ehrmann R S, White E B and Maniaci D 2015 AIAA SciTech, 33rd Wind Energy Symposium AIAA 2015-0489